JOURNAL OF Materials CHEMISTRY

Electrical properties of the oxygen-deficient perovskites, $Ca_2Mn_{2-x}Nb_xO_\gamma$: $0 \leqslant x \leqslant 1.2$, with Mn valence varying from +2.0 to +4.0†

Angela Kruth and Anthony R. West

Department of Engineering Materials, University of Sheffield, Mappin Street, Sheffield, UK S1 3JD

Received 1st December 1999, Accepted 31st May 2000
First published as an Advance Article on the web 27th November 2000

The electrical conductivity of a range of ceramics of general formula $Ca_2Mn_{2-x}Nb_xO_\gamma$, with x and γ as variables, was measured using impedance spectroscopy. All materials were semiconducting but conductivity decreased with both increasing x and decreasing γ, both of which involved a gradual decrease in oxidation state of Mn from +4 in $CaMnO_3$ to +2 in $Ca_2Mn_{0.8}Nb_{1.2}O_{5.8}$. Possible factors that control the conductivity are discussed; electrons in e_g orbitals of Mn appear not to be involved directly; instead, conduction appears to depend either on the degree of t_{2g}–Op_π–t_{2g} orbital overlap or on σ d–p overlap, with donation of electrons from oxygen into the bonds involving e_g orbitals. In both cases, the conductivity is influenced mainly by Mn–O–Mn distances and unit cell dimensions. For compositions of intermediate oxygen content γ, it was difficult to obtain materials that were electrically homogeneous due to oxygen content gradients; thus, samples prepared by partial reduction in H_2 were more heavily reduced at the grain surfaces than in the grain interiors. Since the conductivity was very sensitive to γ, impedance spectroscopy provided a valuable method to investigate oxygen inhomogeneity. Two types of sample inhomogeneity were characterized: those with reduced surfaces and oxidized cores and *vice versa*, those with oxidized surfaces and reduced cores.

Introduction

The perovskite structure is able to tolerate great variations in its stoichiometry, especially oxygen content. Oxygen deficiency has attracted much attention because of its association with a range of phenomena, such as mixed electronic–ionic conduction, superconductivity, giant magnetoresistance and catalytic activity. In perovskites which contain transition metals, especially Cr, Mn, Fe, Co and Ni, the existence of mixed or intermediate valence states is critical for those properties.[1–5]

The $Ca_2Mn_{2-x}Nb_xO_\gamma$ system: $0 \leqslant x \leqslant 1.2$, can accommodate up to 20% vacancies at oxygen sites and Mn occurs in valence states ranging from +2 to +4.[6] Mn and Nb are disordered over the B-sites, at least for composition $x = 1.0$.[7] Depending on the average B-cation composition and oxygen content, two solid solutions form: an extensive orthorhombic $GdFeO_3$-type solid solution over the range $0 \leqslant x \leqslant 1.2$ with zero or small oxygen deficiency, and a closely-related, grossly oxygen-deficient solid solution over the range $0.3 \leqslant x \leqslant 0.8$ with a simple cubic perovskite structure. The unit cell volume, V, and the orthorhombic distortion of the perovskite unit cell due to tilting of MnO_6 octahedra vary with x, γ and Mn valency, as follows: (i) with increasing x (and decreasing Mn valency) at $\gamma = 6$, V and the orthorhombic distortion increase; (ii) on removal of oxygen (and decrease in Mn valency), V increases but the orthorhombic distortion decreases.

Several factors influence the electronic conductivity of transition metal oxides. For the present mixed valence Mn oxides, these include: Mn valence state, Nb content, unit cell size and Mn–O–Mn bond angles. Taguchi[8] studied $CaMnO_{3-\delta}$ with Mn valence ranging from +3.7 to +3.94 and found the conductivity to depend on the oxygen content; on reduction, σ increased, suggesting an n-type conduction mechanism. By contrast, the conductivity of composition $x = 1.0$, with Mn valence in the range +2.8 to +3.0, decreased on reduction; however, oxygen loss occurred preferentially from surface and grain boundary regions leading to oxygen concentration gradients through the samples.

In order to understand which parameters control the conductivity of $Ca_2Mn_{2-x}Nb_xO_\gamma$, a number of fully and partially oxidised samples with $x = 0.5$ and 1.2 have been studied and the results compared with those for $x = 0.0$ and 1.0. For $x = 0.5$, γ varies over the range $5.0 \leqslant \gamma \leqslant 6.0$ and the average Mn valence varies from +2.3 to +3.7; the structure changes from orthorhombic $GdFeO_3$-type to cubic perovskite type with decreasing γ. For $x = 1.2$, the orthorhombic $GdFeO_3$ structure is retained over the range $5.8 \leqslant \gamma \leqslant 6.0$ and the Mn valence varies from +2.0 to +2.5. On reoxidation, $Ca_2Mn_{0.8}Nb_{1.2}O_{5.8}$ forms a poorly characterized, oxygen-rich phase of nominal composition $Ca_2Mn_{0.8}Nb_{1.2}O_{6.2}$ with Mn valence +3.0; this loses the oxygen excess at higher temperatures and reforms single phase $Ca_2Mn_{0.8}Nb_{1.2}O_{6.0}$.

Experimental

Compositions $Ca_2Mn_{2-x}Nb_xO_\gamma$ were prepared, as previously,[6,7] from $CaCO_3$, MnO_2 and Nb_2O_5, which were mixed and fired, first at 900 °C and then at 1250 to 1350 °C in steps of 50 °C with intermediate regrinding. Products were heated finally at 1400 °C for 3 days and quenched in air. Pellets of 3–8 mm diameter and 1–2 mm thickness were cold-pressed at ~200 MPa, sintered overnight at 1400 °C and quenched in air; typical pellet densities were 70–80% of theoretical.

In order to vary the oxygen content, pellets were post-reaction heat-treated in O_2, N_2 and 10% H_2/90% N_2. In high pressure O_2, pellets were heated at 5 °C min^{-1} to 800 °C, held for 16 h and cooled at 2 °C min^{-1} in a Morris Research Furnace, HPS-5015E7. The maximum pressure was ~100 atm

†Basis of a presentation given at Materials Discussion No. 3, 26–29 September 2000, University of Cambridge, UK.

DOI: 10.1039/a909483k

at 800 °C. In flowing N_2, pellets were heated at 10 °C min^{-1} to 1100 °C, held for 10 h and cooled at 2 °C min^{-1}. Heat treatments in H_2/N_2 were carried out in a Stanton Redcroft TG-DTA 1500 which allowed the weight losses to be determined *in situ*. Samples were heated at 10 °C min^{-1} to temperature, cooled at 20 °C min^{-1} to ~350 °C and more slowly thereafter to room temperature. The oxygen partial pressure in these experiments was not buffered since the TG furnace was not leak-proof. The results cannot be related to a particular oxygen partial pressure, therefore, and partially-reduced samples in particular may not have reached a homogeneous, equilibrium state; there was evidence in some cases that grain boundaries were more heavily reduced than grain cores, giving rise to oxygen concentration gradients. Nevertheless, this method was effective as a means of varying the oxygen content and average Mn oxidation state.

Oxygen contents of various pellets were determined from the weight loss during complete reduction of Mn^{3+} and Mn^{4+} to Mn^{2+} in 10% H_2/90% N_2. Pellets were heated at 10 °C min^{-1} until the weight remained constant; it was assumed then that all Mn was reduced to Mn^{2+}. From the total weight loss, the initial oxygen content was calculated. Phase identity and purity were determined by X-ray diffraction, using a Hägg–Guinier camera and CuKα_1 radiation.

For impedance measurements, organo-Ag paste electrodes were attached to opposite pellet faces and dried at 180 °C for 1 h in order to remove organic residue. Thin gold strips were held to the sample by pressure. For measurements over the range 298–793 K, the conductivity jig was inserted in a vertical tube furnace; for measurements at 200–300 K, the jig was fixed inside a Dewar flask containing a dry-ice/acetone liquid bath. An Oxford Optistat Cryostat with an IT C4 temperature controller was employed for data collection at $T \geqslant 83$ K. Measurements in the furnace and dry-ice/acetone were carried out in air; those in the cryostat used N_2. Data were collected over the frequency range 10^{-2} to 10^7 Hz using Solartron 1250/1287 and Hewlett-Packard 4192A LF Impedance Analysers. All data were corrected for sample geometry.

At this point, it is necessary to comment on the correction of electrical data for sample geometry. Conductivities are calculated from resistance data using:

$$R_{\text{corrected}} = \sigma^{-1} = \frac{R_{\text{measured}} A}{l} \quad (1)$$

where l is the thickness and A the area of the pellet; $R_{\text{corrected}}$ is, effectively, the resistivity ρ of the sample, *i.e.* the resistance for unit geometry. In this paper, we prefer the use of $R_{\text{corrected}}$ rather than ρ. Since various components contribute to the overall pellet response, *e.g.* bulk, grain boundary and electrode/sample interface, for accurate analysis each region should be considered separately taking into account the geometry of that region. Usually these geometries are not known and quantitative corrections for geometry cannot be made. Parameters of regions which have been corrected for overall pellet geometry have to be treated with caution, particularly grain boundary conductivities, because grain boundary regions are usually much thinner than bulk regions. Capacitance data are also corrected for overall pellet geometry but, by assuming a typical permittivity value, $\varepsilon' \sim 10$, for different regions of the sample, the dimensions of the regions responsible for the different C values can be estimated approximately. A useful parameter which is independent of geometry is the relaxation time or time constant of each RC element, estimated from $f_{\max}$ data of peaks in Z'', M'' plots. $f_{\max}$ is geometry-independent because $f_{\max} = (2\pi RC)^{-1}$. Since C has the units F cm^{-1} and R has units Ω cm, the product RC is independent of geometry. We have not carried out computer fitting to the impedance data since the main purpose is to establish general trends in composition and temperature dependence rather than accurate quantification of parameters for individual samples.

Results

Composition $x = 0.5$

Electrical characterisation of composition $x = 0.5$ was carried out on four pellets: as-prepared (quenched in air from 1400 °C) and after post-reaction heat-treatment in O_2, N_2 and 10% H_2/90% N_2. In H_2/N_2, it was more difficult to reduce a pellet than a finely powdered sample; the pellet had to be heated to higher temperature in order to obtain the same oxygen content and took longer to equilibrate at a given temperature. It is shown later that the oxygen content may vary significantly throughout a pellet, making it difficult to obtain homogeneous samples during reduction. From TG, the as-prepared pellet and pellets annealed in O_2 and N_2 all had oxygen contents, γ, close to 6.0 and Mn in valence state ~ +3.7. The pellet heated in H_2/N_2 had $\gamma \sim 5.34(2)$ and Mn valence state +2.8.

The three pellets with $\gamma = 6.0$ were highly conducting at room temperature and, therefore, were measured at low temperatures in the cryostat. Fig. 1 shows the impedance complex plane plot for the as-prepared pellet at 83 K. The total resistance was obtained from the intercept with the Z' axis and was $R_{\text{total}} \sim 10.5$ kΩ cm. Note that for these and all subsequent plots, the R and C data were corrected for pellet geometry. Three responses were partially resolved in the plot. The initial assumption was made that these data can be represented by an equivalent circuit composed, ideally, of three parallel RC elements in series, Fig. 1 inset. The low frequency response was assigned to element R_1C_1, the intermediate frequency response to R_2C_2 and the high frequency response to R_3C_3. Arcs, attributed to R_2C_2 and R_3C_3, were poorly resolved and, therefore, R_2 and R_3 values (Table 1) were obtained only approximately; however, R_3 is larger than R_2 and R_1, indicating that R_3C_3 is the most resistive element in this sample at this temperature. From the Z'', M'' spectroscopic plots of the same data, Fig. 2, the high frequency peak had capacitance $C_3 \sim 9$ pF, calculated from the relation

$$C = \frac{\varepsilon_0}{2M''_{\max}} \frac{A}{l} \quad (2)$$

and was assigned to the bulk response. The two other impedance responses had higher capacitances, $C_1 \sim 20$ nF and $C_2 \sim 200$ pF, and were tentatively assigned to electrode–sample contact and grain boundary regions, respectively. The data were not corrected for the blank parallel capacitance of the jig, since it was found to be only a few pF.

If R_1C_1 were associated with a non-ohmic electrode contact, the associated resistance should increase as the applied voltage is decreased. In Fig. 3, a decrease in amplitude of the ac voltage from 1 V to 100 mV led to a significant increase of R_1; R_2 and R_3 did not vary. When Au paste or In–Ga eutectic were applied as electrodes, similar effects were seen but with an even higher value for R_1. Therefore, R_1C_1 represents a non-ohmic contact at the electrode/sample interface. All subsequent measurements were carried out using Ag electrodes and an ac voltage of

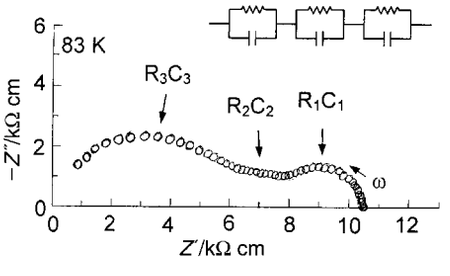

Fig. 1 Composition $x = 0.5$, heated in air at 1400 °C: impedance complex plane plot at 83 K. Inset: equivalent circuit representing three parallel RC elements in series.

Table 1 Composition $x=0.5$; R and C values for as-prepared and heat-treated samples

	O_2 (83 K)	air (83 K)	N_2 (83 K)	H_2/N_2 (250 K)	H_2/N_2 (170 K)
R_{total}/kΩ	11.5	10.5	21.7	185	
R_1/kΩ	2.0(3)	2.6(1)	7.9(7)	10(3)	
R_2/kΩ	2.9(3)	2.2(1)	8.0(7)	35(6)	
R_3/kΩ	6.6(3)	5.7(3)	5.8(7)	140(6)	8100(400)
R_4/kΩ					20(10)[a]
C_1/nF cm^{-1}	8(4)	15(6)	5(2)	200(50)	
C_2/nF cm^{-1}	0.7(2)	1.1(5)	0.05(2)	1.4(4)	
C_3/pF cm^{-1}	10(3)	9(3)	14(4)	9(2)	16(4)
C_4/pF cm^{-1}				4	5(1)[a]

[a]From M'' data.

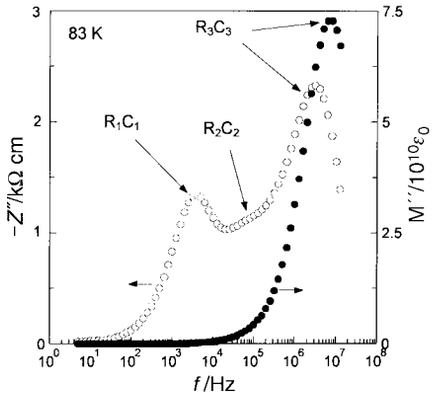

Fig. 2 Composition $x=0.5$, heated in air at 1400 °C: combined spectroscopic Z'', ○, M'', ●, plot at 83 K; same data as used in Fig. 1.

1 V. This reduced the magnitude of R_1 but did not cause any changes to R_2 and R_3.

Impedance plots at 83 K for pellets annealed in O_2 and N_2 were broadly similar to those of the as-prepared sample. For the pellet treated in O_2, R values were similar, Table 1. For the pellet treated in N_2, R_3 changed little but R_1 and R_2 increased significantly and had values similar to R_3. C_1 and C_3 showed little variation after heat treatment in O_2 and N_2, whereas C_2, assigned to the grain boundary region, varied from 0.03–0.07 nF in N_2 to 0.5–0.9 nF in O_2 and 0.6–1.6 nF in air, indicating that the grain boundary layers were relatively thin after treatment in air and O_2, but became thicker in N_2.‡ This appears to be because the grain boundary regions are oxygen-deficient and increase in thickness, due to a small amount of O_2 loss, on heating in N_2.

The fourth pellet, with $\gamma=5.34$, was much more resistive, Table 1. C_3 was similar to the bulk capacitance of oxidised compositions; C_1 and C_2 were larger but from their magnitudes can still be attributed to an electrode/sample interface and a grain boundary, respectively. M'' data, Fig. 4, show a main peak at 3 MHz and a poorly resolved shoulder peak at 200 kHz. The shoulder occurs at a similar position to the main peak of the Z'' spectrum and was attributed to element R_3C_3. The M'' maximum at 3 MHz was assigned to a second bulk element, R_4C_4. Bulk M'' peaks were better separated at lower temperatures which indicates that R_3 has a greater temperature dependence and therefore higher activation energy than R_4 as shown by Arrhenius plots of f_{max} for the Z'' (R_3C_3) and M'' (R_4C_4) peaks, Fig. 5. If it is assumed that C_3 and C_4 are independent of temperature, then the activation energies, E_a, for f_{max} correspond to those for the respective R values. E_a for R_4C_4 (0.13 eV) is smaller than for R_3C_3 (0.21 eV) and higher than for R_3C_3 in fully oxidised samples (0.09 eV, see later).

‡Since C data are corrected for overall pellet geometry and the permittivity values, ε', of different regions of the pellet are likely to be similar, then the capacitance values give an approximate idea of the thickness of each region.[9]

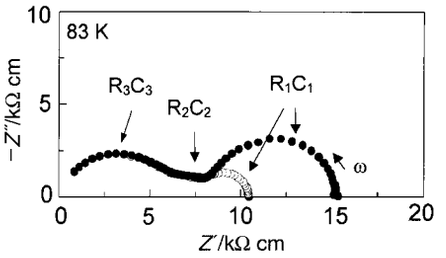

Fig. 3 Composition $x=0.5$, heated in air at 1400 °C: data at 83 K for applied ac voltages of 100 mV, ●, and 1 V, ○.

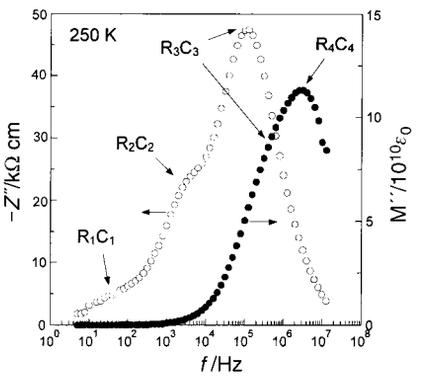

Fig. 4 Composition $x=0.5$, heat-treated in H_2/N_2 at 580 °C: combined spectroscopic M'', Z'' plot at 250 K.

Values of R_4 and C_4 calculated from M'' data are shown in Table 1. R_4 is much smaller than R_3 and R_3C_3 is therefore the more resistive bulk region. From the observed dependence of resistance on oxygen content, it appears that R_3C_3 corresponds to the outer grain region which is more reduced than the inner R_4C_4 grain core. The value of C_4 is smaller than that of C_3;

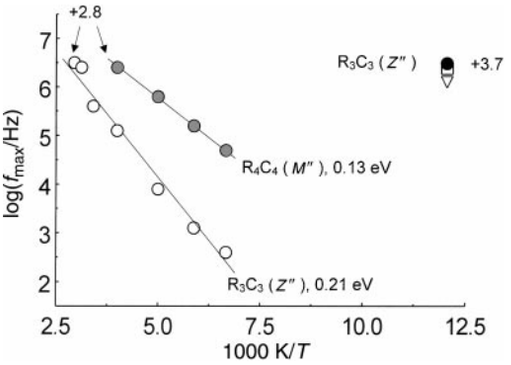

Fig. 5 Arrhenius plots of log f_{max} for bulk responses, R_3C_3 and R_4C_4, of composition $x=0.5$, heat-treated in air, ●, O_2, □, N_2, ▽, and H_2/N_2; R_3C_3 (white circles) and R_4C_4 (grey circles). Average Mn valence states, +3.7 and +2.8, for different data sets are indicated.

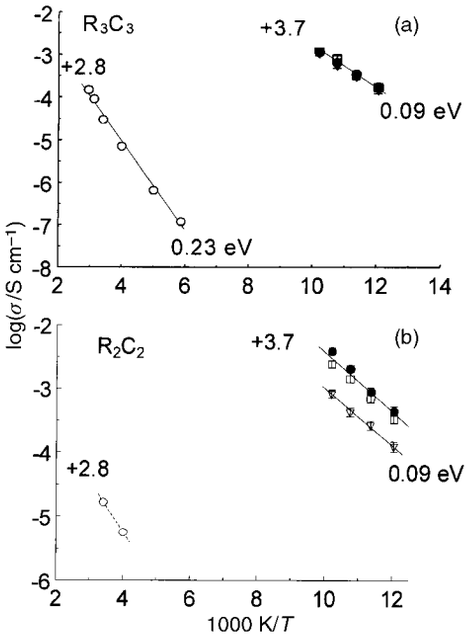

Fig. 6 Arrhenius plots of (a) bulk and (b) grain boundary conductivities, σ_3 and σ_2, of composition $x=0.5$, heat treated in air, ●, O_2, □, N_2, ▽ and H_2/N_2, ○.

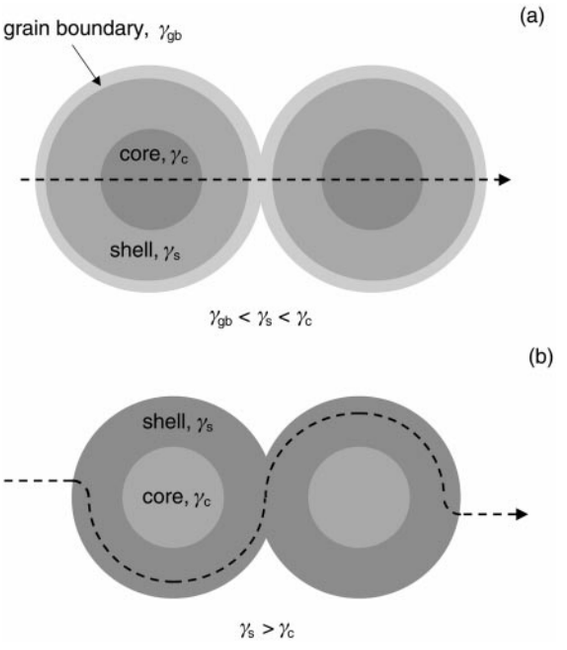

Fig. 7 Conduction pathways through inhomogeneous grains: (a) partially reduced grain after heat-treatment of a fully oxidised sample in H_2/N_2; (b) partially re-oxidised grain after heating of a reduced composition in air.

consequently, the reduced, outer region is thinner than the less-reduced core.

Bulk and grain boundary conductivities, σ_3 and σ_2, of all four samples are plotted in Arrhenius format in Figs. 6a and b: note that the σ_2 data refer to the overall geometry of the pellet and not to that of the grain boundary region. Samples annealed in air, O_2 and N_2 with Mn average valence state +3.7 had similar bulk conductivities and E_a, ~0.09 eV. After reduction in H_2/N_2 to give Mn average valence state +2.8, σ_3 decreased drastically and E_a increased to ~0.23 eV although the Arrhenius plot may be slightly curved. The variation in activation energies between oxidised and reduced samples may either indicate the existence of distinct conduction mechanisms in samples with different Mn average valencies, or that the difficulty of electron hopping between adjacent Mn atoms is composition-dependent. This is discussed later (Fig. 11) where it is concluded that a single conduction mechanism occurs.

Grain boundary conductivities, σ_2, Fig. 6b, are similar for samples heated in air and O_2, but decrease significantly in N_2 and greatly in H_2/N_2. E_a values are similar for samples heated in air, O_2 and N_2 (~0.09 eV), but much larger in H_2/N_2. Since activation energies for bulk and grain boundary regions in air, O_2 and N_2 are similar, 0.09 eV, the conduction mechanism is the same in both regions.

A schematic model for conduction through partially reduced grains is shown in Fig. 7a. Grain shells (R_3C_3) are more resistive than cores (R_4C_4) and where possible, charge carriers travel through the inner bulk regions. It is shown later that this is not always the case and the conduction path may vary greatly depending on the thermal history. XRD of the reduced pellet showed a cubic pattern, similar to those for oxygen-deficient samples with $x=0.5$.[7] However, the lines were diffuse, probably due to variation of γ within the sample bulk.

Composition $x=1.2$

In Nb-rich compositions, the oxygen content varies over a smaller range than in Mn-rich compositions.[7] Two pellets were prepared: the as-prepared pellet had $\gamma=6.0$ and Mn valence state +2.5; the other pellet was reduced in H_2/N_2, had $\gamma=5.8$ and all Mn reduced to Mn^{2+}. Note that +2.5 is not the highest average valence state of Mn which can be achieved for this cation composition; on heating the reduced sample in air, the average Mn oxidation state increases to +3.0 to yield a metastable phase of composition $Ca_2Mn_{0.8}Nb_{1.2}O_{6.2}$. This excess oxidation is important for the interpretation of impedance data, as seen later.

The $-Z''$, Z' plane for the as-prepared pellet at 278 K showed a large arc with $R\sim3.9$ MΩ cm and $C\sim2(3)$ pF, which was assigned to the bulk region, R_3C_3. A second, small arc at low f had ~10 nF, and was attributed to either the grain boundary, R_2C_2, or the electrode/sample interface, R_1C_1; it was not investigated further.

The reduced pellet with $\gamma=5.8$ was the most resistive sample investigated. The $-Z''$, Z' plane (not shown) had a single arc with $R_3\sim9.4$ MΩ cm and $C\sim5$–9 pF at 508 K, Table 2. M'' data (not shown) showed a single, symmetric peak attributed to R_3C_3; in this case, the sample bulk appeared not to separate into regions of different oxygen content on reduction.

C_3 showed little variation with temperature and was 2–7 pF for as-prepared and reduced pellets. Bulk conductivities, σ_3, are given in Arrhenius format in Fig. 8. For $\gamma=6.0$, data, *, fell on a straight line with $E_a\sim0.39$ eV and were reversible on cooling. Data for $\gamma=5.8$, however, showed more complex behaviour, attributed to partial reoxidation of the sample ⩾400 °C. On first heating, ●, data fell on a fairly straight line, possibly slightly curved, with activation energy ~0.84 eV. On annealing at 400 °C overnight, its conductivity increased (→) and variable temperature data ■, ○ fell on a second straight line with decreased $E_a\sim0.55$ eV. At $T>400$ °C, a further jump in conductivity occurred, – – –, with a new activation energy of ~0.23 eV. In order to exclude any possible influence of the Ag electrode on these conductivity data, especially for samples heated >400 °C, a second set of experiments was performed in which electrodes (of InGa alloy) were added only after the heat

Table 2 Composition $x=1.2$; R and C values for as-prepared, $\gamma=6.0$, and reduced, $\gamma=5.8$, pellet

	Air (278 K)	Air (472 K)	H_2/N_2 (508 K)
$R_{1,2}$/kΩ		2.6(1)	
R_3/kΩ	3900(300)	4.8(3)	9400(400)
$C_{1,2}$/nF cm^{-1}		10(2)	
C_3/pF cm^{-1}	2(3)		7(2)

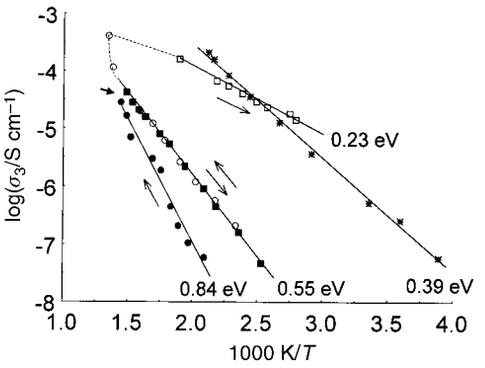

Fig. 8 Arrhenius plots and activation energies of bulk conductivities, σ_3, for compositions $x=1.2$: $\gamma=6.0$, *, and $\gamma=5.8$ during first (filled symbols) and second (open symbols) heating, ● ○, and cooling, ■ □, cycles.

treatments >400 °C. Similar trends to those shown in Fig. 8 were obtained, thus showing that the conductivity increases were unaffected by the electrode. From the general trend of increased conductivity with increased oxygen contents, some oxidation of the sample had clearly occurred at >400 °C. However, X-ray patterns of the initial, reduced sample and after the second cooling were identical, and so oxygen uptake was probably limited to the grain boundaries, forming relatively thin conductive regions. C_3 remained small and was similar to that in the as-prepared sample, Table 2. From this, we suggest that charge carriers travel along conductive surface regions, bypassing the more resistive inner bulk region, Fig. 7b; thus, C_3 still refers to the bulk of the sample, which includes both the conductive surface layers and the less conductive grain cores.

The activation energy decreased greatly during reoxidation of the grain surfaces, Fig. 8, so much so that, after heating >400 °C, it was smaller than that of the as-prepared sample. Since E_a decreases with increasing oxygen content, it seems likely that the oxygen content in the outer surface region was larger, *i.e.* $\gamma>6.0$, than in the as-prepared sample. It was shown previously[6] that an anomalously high oxygen content is achieved on oxidation at intermediate temperatures, ~750 to 1000 °C; these are much higher temperatures than achieved during the present impedance measurements, 400 to 470 °C, which may therefore be high enough to oxidise the grain boundary/grain surfaces but not the entire sample.

$CaMnO_{3.0}$

A pellet of $CaMnO_{3.0}$ with Mn valence state +4.0 was prepared.[6] The $-Z''$, Z' plane at 83 K is given in Fig. 9 for two applied voltages, 100 mV and 1 V. The total resistance was ~70 Ω cm and varied greatly with applied voltage; thus the arcs seen in Fig. 9 represent the electrode/sample interface. The resistance of the sample, given by the high frequency intercept of the arcs, is ~42 Ω. The electrical properties could not be further investigated with the frequencies available and it is not known whether any grain boundary resistance contributed to the sample resistance, but certainly the bulk resistance is ⩽42 Ω at 83 K. This is much lower than reported for $CaMnO_{3-\delta}$ by Taguchi ($R\sim10$ kΩ cm at $T\sim160$ K).[8] The reason for this discrepancy is not known; it may involve differences in oxygen content in the different samples.

Discussion

In the present family of materials, complex electrical characteristics were apparent but some general trends may be seen: (i) with increasing x, and decreasing Mn valency at $\gamma=6.0$, both R and E_a increase, Fig. 10; (ii) with decreasing γ and Mn valency at constant x, both R and E_a increase (Figs. 6 and 10

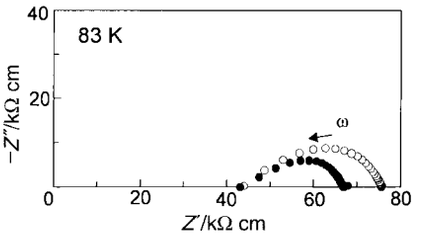

Fig. 9 $CaMnO_{3.0}$, prepared in O_2: impedance complex plane plot at 83 K, with applied ac voltages of 100 mV, ○, and 1 V, ●.

and ref. 7). From the composition and temperature dependence of conductivity, deductions about the conduction mechanism may be made and the role of parameters that influence the conductivity may be considered.

Conduction mechanisms

For all the materials studied, apart from $CaMnO_3$ for which we have few data, the conductivity is thermally activated and the Arrhenius plots are generally linear. Although σ and E_a vary with composition, the conductivity pre-exponential factor A, from $\sigma=A\exp(-E_a/kT)$, is almost constant, Fig. 11. Hence, the number of mobile carriers is constant and the conductivity is governed entirely by the ease of hopping, E_a. The conductivity is therefore intrinsic since there is no evidence for any extrinsic region in which carrier concentration varies. Since the conductivity is thermally activated and intrinsic, the mechanism involves the hopping of localised electrons or small polarons, rather than conduction through delocalised bands. Since the carrier concentration is independent of composition, it is inappropriate to refer to the conduction mechanism as p-type, even though the conductivity increases with increasing average oxidation state of Mn.

Mn 3d orbital interactions

The details of the conduction mechanism can be discussed in terms of electron configurations of Mn ions and possible interactions involving the 3d orbitals. If we assume a high spin configuration for octahedrally coordinated Mn, consistent with magnetic susceptibility data for Ca_2MnNbO_γ,[7] and neglecting any Jahn–Teller splitting, then the energy level diagrams for the various Mn ions are: Mn^{2+}: $t_{2g}^3\,e_g^2$; Mn^{3+}: $t_{2g}^3\,e_g^1$; Mn^{4+}: $t_{2g}^3\,e_g^0$. It is usually assumed that the electrons responsible for conductivity are those in the highest occupied levels, since electrons in lower levels are increasingly localised or in levels that are fully occupied. For example, the electronic conduction in GMR manganates with Mn in a mixed +3/+4 valence state is explained by assuming that t_{2g}^3 electrons are localised with a spin of $S=3/2$, while e_g electrons are strongly hybridised with the oxygen 2p state, Fig. 12a, forming a σ d–p bond between

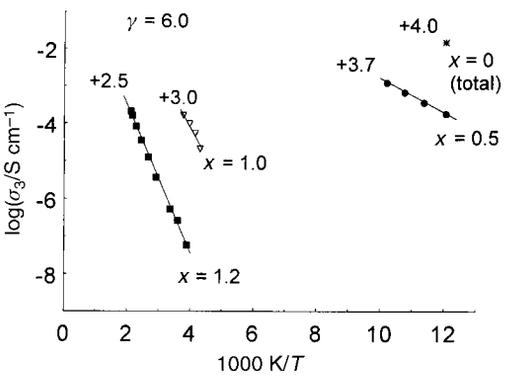

Fig. 10 Arrhenius plots of bulk conductivities, σ_3, for fully oxidised compositions, $Ca_2Mn_{2-x}Nb_xO_{6.0}$: $x=0.5$, ●; $x=1.0$, ▽; $x=1.2$, ■. Total σ for $CaMnO_{3.00}$, *.

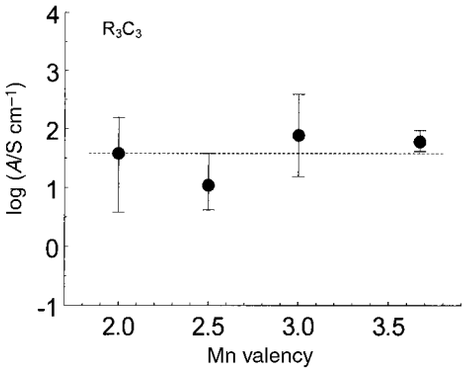

Fig. 11 Pre-exponential factor, A, as a function of Mn valency.

Mn and O;[1,10,11] e_g electrons hop from Mn^{3+} to Mn^{4+} *via* the bridging oxygen, so that effectively Mn^{3+} and Mn^{4+} ions change places. The difficulty in applying this model to the present materials is that conductivity is greatest when Mn is in the +4 state, for which the e_g orbitals are empty. If, however, some partial occupancy of e_g orbitals occurs, through contribution of oxygen 2p electrons to the σ d–p bonds, then would be forced to conclude that, effectively, oxygen 2p electrons are responsible for the high conductivity in $CaMnO_3$.

Alternatively, the t_{2g} rather than the e_g electrons may be responsible for the conductivity. The relative disposition of t_{2g} orbitals on adjacent Mn atoms in a simple perovskite structure suggests two possible modes of orbital interaction.

First, t_{2g} orbitals may overlap with the O p_π orbitals in directions parallel to the unit cell edges, Fig. 12b. This situation is comparable to that in tungsten bronzes, A_xWO_3 with A = alkali metals or protons,[12,13] in which t_{2g}–p_π–t_{2g} overlap is responsible for metallic conductivity. WO_3 ($x=0$) has an empty W 5d (t_{2g}) band and is insulating. Reduction of W^{6+} to W^{5+} (increasing x) introduces electrons into the 5d (t_{2g}) band and at high x, a Mott transition to a metallic state occurs. This model may be considered for the present system in which the t_{2g} band is half-filled for d^3, d^4 and d^5 high spin Mn; conduction through

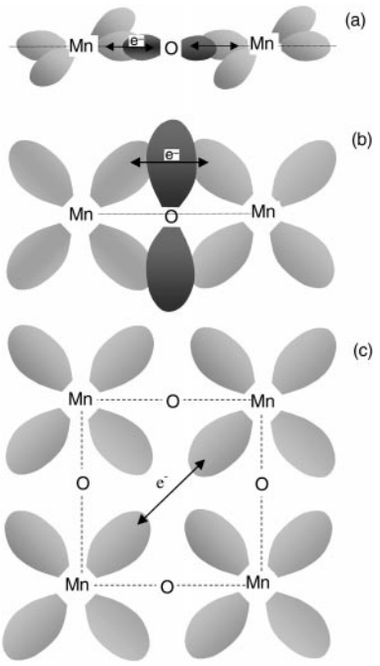

Fig. 12 Possibilities of Mn d-orbital interactions in a simple cubic $AMnO_3$ perovskite structure: (a) e_g–p_σ–e_g overlap of Mn ions with oxygen (σ-bond), (b) t_{2g}–p_π–t_{2g} overlap of Mn ions with oxygen (π-bond) and (c) direct t_{2g}–t_{2g} overlap between Mn ions across the unit cell face diagonal.

the t_{2g} orbitals is possible in all three cases but the materials are semiconducting rather than metallic, which might indicate that the t_{2g}–p_π–t_{2g} orbital overlap is poor. The increase of conductivity on oxidation could correlate with an increase in t_{2g}–p_π–t_{2g} orbital overlap due to reduction in unit cell dimensions. Factors that influence orbital separation are discussed later.

It might also be considered whether t_{2g} orbitals interact directly across the unit cell face diagonal, as occurs in some rocksalt structures, *e.g.* TiO, Fig. 12c. In TiO, the t_{2g} conduction band, resulting from direct t_{2g}–t_{2g} overlap, is 1/3 full (d^2 Ti) and gives rise to metallic conduction.[12] In the present system, the Mn–Mn distance across the cell face diagonal is larger than in rocksalt structures (approximately twice as long) and direct t_{2g}–t_{2g} overlap appears unlikely.

To a first approximation, then, it is concluded that conduction in the present materials may involve either the t_{2g} electrons through t_{2g}–p–t_{2g} orbital overlap or the e_g orbitals through σ d–p orbital overlap, with electrons provided primarily by oxygen. Enormous variations in conductivity are seen with changing valence of Mn; since the number of t_{2g} and oxygen p electrons is constant, the activation energy and, hence, the conductivity must be controlled by the separation of orbitals on adjacent atoms.

Mn 3d-orbital separation

In considering the separation of orbitals on adjacent atoms, two factors are potentially important: the size/charge of Mn and the unit cell dimensions. First, the idealised cation radius of Mn in octahedral coordination decreases on oxidation, from 0.83 Å (Mn^{2+}) to 0.53 Å (Mn^{4+}).[14] Consequently, with increasing charge of Mn, the d electrons should be held more tightly to the nucleus, the orbital extent and overlap should decrease and conductivity through the d orbitals should decrease. The exact opposite occurs, however, as the conductivity increases with Mn oxidation state. Alternatively, with increasing occupation of e_g orbitals in the sequence Mn^{4+}–Mn^{3+}–Mn^{2+}, the ionic size of Mn increases but the spatial extent of the t_{2g} orbitals might decrease because of electron–electron repulsion, and hence t_{2g} orbitals on adjacent Mn ions become more separated. The latter situation would be consistent with the present data; conductivity is lowest when all Mn is in valence state +2 and possesses the highest number of e_g electrons.

Second, an increase in unit cell dimensions must increase interatomic distances and, therefore, increase the orbital separation. In the present materials, the unit cell expands on increasing x and decreasing γ, both of which are associated with a decrease in Mn valence. Fig. 13 shows that activation energies increase non-linearly with the average perovskite unit cell dimension, $a_p = \sqrt[3]{V}$. For small interatomic distances with a higher degree of orbital overlap, E_a is relatively small and

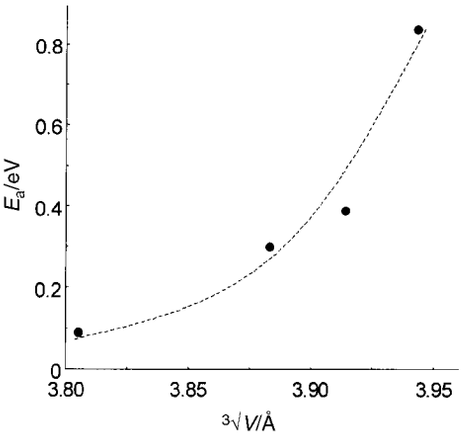

Fig. 13 Variation of E_a with perovskite unit cell dimension, $\sqrt[3]{V}$.

varies little with unit cell size; for large interatomic distances and poor orbital overlap, E_a depends increasingly strongly on a_p. This simple correlation, Fig. 13, indicates that interatomic distance may be the main factor that determines electronic conductivity in the present system.

Tilting of octahedra in the $GdFeO_3$-type structure

We may also consider the possible influence of non-linearity of Mn–O–Mn bonds due to tilting of MnO_6 octahedra in the orthorhombic solid solutions with the $GdFeO_3$ structure and the absence of tilting in the reduced, cubic solid solutions. Cubic structures with a Mn–O–Mn bond angle of 180 °C would maximise the Mn–O–Mn σ and π orbital interactions. In structures with tilted octahedra, the Mn–O–Mn bond angles deviate from 180 °C, give poorer σ and π orbital overlap and increased localisation of d-electrons.[15,16]

Conductivity data do not indicate a major influence of octahedral tilting on conductivity. For $x=0.5$, as oxygen is removed from the structure, the orthorhombicity decreases and a transition to a simple cubic structure occurs. At the same time, a decrease in conductivity with increased activation energy is observed which is perhaps the opposite of what would be predicted. Also, there is no obvious correlation between the degree of orthorhombicity (greatest for $x=1.2$, $\gamma=6$) and conductivity (greatest for $x=0$, $\gamma=6$).[7,17,18]

Oxygen vacancies

Some compositions were oxygen-deficient and contained 3–11% oxygen vacancies. The role of oxygen vacancies may be discussed in terms of e_g–p_σ–e_g or t_{2g}–p_π–t_{2g} orbital overlap which, on removal of oxygen from the structure, may prevent d–p–d interactions and interrupt electron hopping between the metal ions, leading to low conductivity. This is consistent with the observed decrease of conductivity with increasing oxygen deficiency.

Nb content

We can discount any major effect of inert Nb^{5+} ions on the conductivity, provided that there are sufficient Mn–Mn or Mn–O–Mn close contacts to give a 3D hopping pathway through the structure for electrons. Assuming a random distribution of Mn and Nb over the B-sites, the question of whether Mn–Mn or Mn–O–Mn interactions can occur depends on composition and is essentially a percolation problem; provided there is sufficient Mn present to provide a percolation pathway, then dc conduction is possible and should be fairly insensitive to the Nb content. For the present materials, the entire range, $0 \leqslant x \leqslant 1.2$, is within the percolation limit.

High spin Mn^{3+}

We may also consider whether, in situations where all Mn is in the +3 state, any anomalies in the electrical properties are expected. There is some evidence for this in f_{max} data for the bulk conductivities shown in Fig. 14. The activation energy for the data set with valence state +3 is anomalously high and out of sequence with the remaining data; it could be that, for this composition, the unit cell is locally distorted, perhaps with a structural elongation associated with a local Jahn–Teller effect, and this gives rise to a small increase in Mn–Mn separations, and hence an increase in activation energy.

Conclusions

The variation of conductivity with composition in the $Ca_2Mn_{2-x}Nb_xO_\gamma$ system may be discussed in several ways. The increase of conductivity on oxidation of Mn is often explained by the concept of p-type hopping conduction,[19] but this model cannot explain the high values of conductivity when

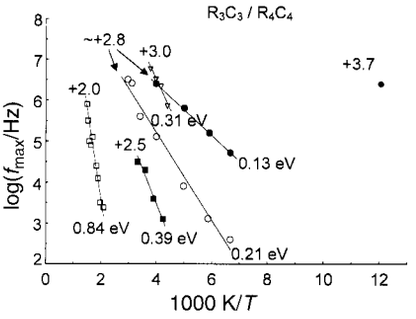

Fig. 14 Arrhenius plots of log f_{max} (obtained from M'' or Z'' data) for bulk responses in the $Ca_2Mn_{2-x}Nb_xO_\gamma$ system: $x=0.5$, $\gamma=6.0$, ●, and $\gamma=5.34$ with the two bulk responses, ○ and ●; $x=1.0$, $\gamma=6.0$, ▽; $x=1.2$, $\gamma=6.0$, ■, and $\gamma=5.8$, □.

Mn has valency +4.0. We found no evidence that Mn electrons in the e_g orbitals are responsible for conduction. Instead, either oxygen p electrons forming σ d–p bonds with e_g orbitals or t_{2g} electrons linking through oxygen p_π orbitals are the conducting species. Direct t_{2g}–t_{2g} orbital interactions between Mn ions across the unit cell face diagonal are unlikely because of the large Mn–Mn interatomic distance. Conductivities depend on the degree of d–p orbital overlap, which is influenced directly by Mn–O–Mn distances and, hence, unit cell dimensions. There was no systematic dependence of conductivity on Mn–O–Mn bond angle but the octahedral tilt angles may be too small to have a significant effect.

The electrical characteristics of ceramic samples depended very much on sample history. Samples that were partially reduced [*in situ* reduction in H_2/N_2 in TG experiments] were particularly complex, probably because reduction commenced at the grain surfaces, giving rise to oxygen gradients and non-equilibrium structures. Similarly, reduced samples that were allowed to partially reoxidise gave rise to samples that were electrically inhomogeneous. In both cases, impedance measurements provided a sensitive indicator of sample inhomogeneity. Most of the data reported here are for samples that were fully oxidized or fully reduced; their results provided a framework on which to explain the behaviour of more complex inhomogeneous samples of intermediate oxygen content.

References

1 C. N. R. Rao, A. K. Cheetham and R. Mahesh, *Chem. Mater.*, 1996, **8**, 2421.
2 R.-F. Huang and W. Y. Howng, *J. Mater. Res.*, 1996, **11**, 3077.
3 W. T. A. Harrison, T. H. Lee, Y. L. Yang, D. P. Scarfe, L. M. Liu and A. J. Jacobson, *Mater. Res. Bull.*, 1995, **30**, 621.
4 B. Ma and U. Balachandran, *J. Electroceram.*, 1998, **2**, 135.
5 P. Hagenmuller, M. Pouchard and J. C. Grenier, *Solid State Ionics*, 1990, **43**, 7.
6 A. Kruth, U. Guth and A. R. West, *J. Mater. Chem.*, 1999, **9**, 1579.
7 A. Kruth, M. Tabuchi, U. Guth and A. R. West, *J. Mater. Chem.*, 1998, **8**, 2515.
8 H. Taguchi, *Phys. Status Solidi A*, 1985, **88**, K79.
9 J. T. S. Irvine, D. C. Sinclair and A. R. West, *Adv. Mater.*, 1990, **2**, 132.
10 J. B. Goodenough, *Prog. Solid State Chem.*, 1971, **5**, 149.
11 P. D. Battle, D. E. Cox, M. A. Green, J. E. Millburn, L. E. Spring, P. G. Radaelli, M. J. Rosseinsky and J. F. Vente, *Chem. Mater.*, 1997, **9**, 1042.
12 J. A. Duffy, *Bonding, Energy Levels & Bands in Inorganic Solids*, Longman Scientific & Technical, Essex, 1990.
13 N. S. P. Bhuvanesh and J. Gopalakrishnan, *J. Mater. Chem.*, 1997, **7**, 2297.
14 R. D. Shannon, *Acta Crystallogr., Sect. A*, 1976, **32**, 751.
15 H. Taguchi, *J. Solid State Chem.*, 1996, **124**, 360.
16 P. M. Woodward, *Acta. Crystallogr., Sect. B*, 1997, **53**, 44.
17 A. Kruth and A. R. West, unpublished work.
18 S. K. Mishra and S. Satpathy, *Phys. Rev. B*, 1998, **58**, 7585.
19 J. Töpfer, J. P. Doumerc and J. C. Grenier, *J. Mater. Chem.*, 1996, **6**, 1511.